Chinese Chemical Letters 37 (2026) 112411

Contents lists available at ScienceDirect

Chinese Chemical Letters

journal homepage: www.elsevier.com/locate/cclet

Sustainable organic salt-derived porous carbons: Activation/self-activation fabrication, dimensional control and environmental applications

Mingxing Shi[a,1], Jiahui Liu[b,1], Wei Jin[b], Zahira Bano[c], Yubo Pan[c], Jianzhe Ma[d], Xu Wu[a], Huijuan Jia[c,*], Guolin Tong[a,*]

[a] College of Light Industry and Food Engineering, Nanjing Forestry University, Nanjing 210037, China
[b] School of Environmental Science and Engineering, Suzhou University of Science and Technology, Suzhou 215009, China
[c] School of Chemistry and Chemical Engineering, Nanjing University of Science and Technology, Nanjing 210094, China
[d] Nanjing Institute of Environmental Science, MEE, Key Laboratory of Pesticide Environmental Assessment and Pollution Control, Nanjing 210042, China

ARTICLE INFO

Article history:
Received 27 May 2025
Revised 9 December 2025
Accepted 12 January 2026
Available online 14 January 2026

Keywords:
Sustainable organic salts
Green activation strategy
Porous carbons
Dimensional architecture control
Environmental applications

ABSTRACT

Although porous carbons (PCs) are promising materials for environmental remediation, their synthesis strategies face high cost, strong device corrosion and severe environmental hazards. This review overviews sustainable organic salt-derived PCs (OAPCs), emphasizing their dual role as activators and self-activators. Meanwhile, six different organic salts are identified for the unique decomposition pathways and activation mechanisms, governing hierarchical porous formation, heteroatom doping, *etc.* Crucially, the dimensional control of OAPCs from 0D to 3D is min discussed, which favors optimizing ion transport and surface accessibility. The environmental applications of OAPCs are further assessed, proving high potential value in the adsorption, capacitive deionization (CDI), peroxymonosulfate (PMS) activation, electro-Fenton (EF) and microwave absorption. These advancements mainly rely on the tailored morphology and porosity, high conductivity and improved hydrophilicity. Overall, this review provides new insights into sustainable OAPCs, bridging fundamental mechanisms to practical environmental solutions.

© 2026 Published by Elsevier B.V. on behalf of Chinese Chemical Society and Institute of Materia Medica, Chinese Academy of Medical Sciences.

1. Introduction

In the background of accelerated global industrialization and urbanization, environmental pollution has been a huge challenge of growing complexity and severity, posing significant threats to ecological equilibrium and human health [1,2]. Critical issues ranging from water quality deterioration induced by freshwater scarcity to air/soil contamination from diverse pollutant emissions (*e.g.*, pharmaceuticals, heavy metals, nuclides, chloride, CO_2 and SO_2) and electromagnetic radiation from ubiquitous electronic devices, insistent need for effective mitigation strategies [3–5]. Such multifaceted environmental pressures inherently necessitate the development of advanced porous materials with tunable properties and broad applicability in the fields of detection, adsorption, catalysis and absorption. Thus, various functional porous materials have been exploited, *e.g.*, Mxene, hydrotalcite, metal-organic frameworks (MOFs), covalent organic frameworks (COFs) and porous carbons (PCs), as the core for treating various environmental issues [6–8].

Currently, PCs have emerged as promising candidates for environmental applications due to their low cost, sustainability, tunable physicochemical properties and high structural stability [9,10]. Well-designed PCs deliver unique hierarchical porous structures, improved hydrophilicity, enhanced conductivity and superior mechanical properties [11,12]. According to IUPAC classification, porosity is categorized into micropore (<2 nm), mesopore (2-50 nm) and macropore (>50 nm) [13]. Normally, macropores act as electrolyte/gas highways. Mesopores optimize mass transport rate, while micropores are effective active sites [14]. Advanced PC-based materials such as carbon aerogels prove hierarchical porosity integrated with broad pore size distribution that combine high surface accessibility with efficient reactant transport [15]. Novel strategies involving heteroatom doping (*e.g.*, N, S, P, B, Fe, Co) further reinforce the property adjusting electronic/lattice configurations to activate active zones, while self-supporting designs realize rapid recovery of materials [16]. These engineering, particularly hierarchical porous structures, high specific surface area (S_{BET}), large pore volume (V_{pore}) and splendid stability, pose

* Corresponding authors.
E-mail addresses: huijuanjia@njust.edu.cn (H. Jia), gtong@njfu.edu.cn (G. Tong).
[1] These authors contributed equally to this work.

https://doi.org/10.1016/j.cclet.2026.112411
1001-8417/© 2026 Published by Elsevier B.V. on behalf of Chinese Chemical Society and Institute of Materia Medica, Chinese Academy of Medical Sciences.

PCs as core materials [17]. Current applications span sensing, adsorption, capacitive deionization (CDI), peroxymonosulfate (PMS) activation, electro-Fenton (EF) and microwave absorption, where the unique combination of morphology, porosity and stability addresses key challenges in the detection and removal of pollutants [18–20].

Normally, typical manufacturing strategies for PCs include the hydrothermal-activation method, carbonization-activation method, template method and gas exploiting method [21,22]. However, these strategies frequently encounter challenges associated with using toxic solvents (*e.g.*, methanol and DMF), costly raw materials, complex preparation craft and risky HF washing, particularly when employing hazardous chemicals like KOH, H_3PO_4 and $ZnCl_2$, *etc.* [23,24]. These strongly corrosive activators, especially high-powered KOH (detailed activation mechanism see Text S1, Eqs. S1-S5 and Fig. S1 in Supporting information), not only raise device corrosion and environmental concerns *via* corrosive waste generation but also hinder further commercial production. Thus, there is an urgent need to develop an eco-friendly, simple and scalable synthesis strategy.

Notably, organic salt activation/self-activation is a green and effective strategy to exploit PCs, but suffers from less research [25,26]. Differently, organic salt-derived PCs (OAPCs) can often be fabricated *via* only one-step pyrolysis and have high carbon yields due to their mild and efficient activation effect. Also, organic salts have copious types (*e.g.*, potassium, sodium and zinc), which can meet the preparation needs of single- or hierarchical-porous OAPCs [27,28]. More importantly, organic salts could realize the precise design of OAPCs in diverse dimensions from 0D to 3D by using the decomposition, catalysis and pore-forming effects of metal ions, anions and organic ligands in their composition during pyrolysis [29,30]. The unique effect makes OAPCs have highly customized features, thus meeting the strictly needs of material morphologies and structures for diverse environment applications.

Herein, the review overviews sustainable OAPCs, stressing their dual effect as activators/self-activators. Six diverse organic salts are studied for their decomposition pathways and activation mechanisms, governing hierarchical pore formation and heteroatom doping. Also, the mechanism identification between organic salts and OAPCs was disclosed. More importantly, the dimensional control of OAPCs from 0D to 3D is minute discussed, reinforcing ion transport and active site accessibility. Eventually, OAPCs show high potential in adsorption, CDI, PMS activation, EF and microwave absorption, being mainly driven by adjustable morphology, controllable pore structure, enhanced conductivity and optimized hydrophilicity. The corresponding schematic illustration is given in Fig. 1.

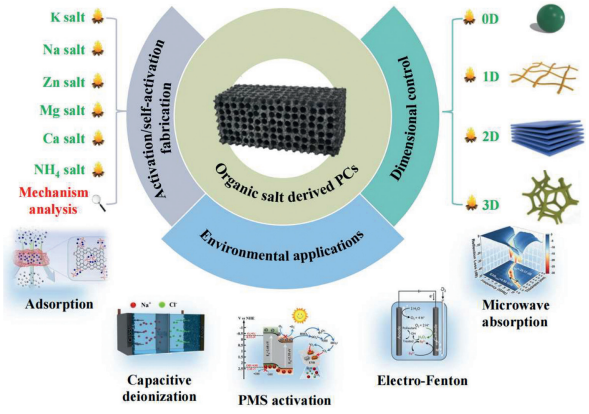


Fig. 1. Schematic illustration of emerging OAPCs: Activation/self-activation fabrication, dimensional control and environmental applications.

2. Sustainable organic salt activation/self-activation strategy

Organic salts, as both activators and self-activators, abundant and featured by specific chemical structures and unique activation mechanisms [31], favor developing OAPCs with high S_{BET} and large porosity, while also enabling N or S doping [32]. The section systematically discusses the effect of six diverse organic salts in the synthesis of OAPCs. By researching the specific activation mechanisms, we can more deeply understand the roles in building hierarchical porosity and improving surface chemical property, realizing effective construction of high-performance OACPs.

2.1. Organic potassium salt

2.1.1. Potassium citrate ($C_6H_5K_3O_7$)

$C_6H_5K_3O_7$ is the most widely used organic salt. It can generate OAPCs either *via* self-activation or by activating other precursors [33]. Normally, $C_6H_5K_3O_7$ can decompose at temperatures below 650 °C to form K_2CO_3 (Eq. 1), which then follows the same activation pathways as K_2CO_3 (Eqs. S2-S5 in Supporting information)) [34]. Structurally, it features copious -COOH and -OH, favoring the release of active gases like CO_2 and H_2O during pyrolysis. Besides, -COOH can promote crosslinking reactions, thus inducing more porosity. The combination of high reactivity, inherent structure of the precursor and effective K_2CO_3 induces $C_6H_5K_3O_7$-based OAPCs delivering excellent S_{BET} and plentiful microporous [35].

$$2C_6H_5K_3O_7H_2O \rightarrow 3K_2CO_3 + 9C + 7H_2O \quad (1)$$

$C_6H_5K_3O_7$-based OAPCs often have a high micropore proportion. However, their carbon skeleton is relatively closed. This can to some extent hinder the target ions or molecules from diffusing into the internal active sites [36]. $C_6H_5K_3O_7$ self-activation-derived OAPCs designed by Tian *et al.* [37] indicated a superior S_{BET} of 2337.1 m^2/g. However, S_{micro} and V_{micro}/V_{pore} were 2008.6 m^2/g and 89.1 %, respectively (Figs. 2a and b).

2.1.2. Potassium gluconate ($C_6H_{11}KO_7$)

$C_6H_{11}KO_7$ is another novel organic salt for the synthesis of OPACs, but suffers from less research compared with $C_6H_5K_3O_7$ [38]. Activation mechanism studies uncover that it is chemically stable and has analogous thermal decomposition pathways to K_2CO_3 (Eqs. S2-S5). Specifically, $C_6H_{11}KO_7$ first decomposes into K_2CO_3 (Eq. 2), which then joins in the structural evolution of the carbon skeleton by chemical etching and intercalation effect [39]. Attributed to the synergistic effects of gaseous products and alkaline species during pyrolysis, the multistage activation favors a rapid increase in both S_{BET} and porosity.

$$2C_6H_{11}KO_7 \rightarrow K_2CO_3 + 11C + 11H_2O \quad (2)$$

$C_6H_{11}KO_7$ owns copious -CHO and -COOH [41]. Its structural simplicity and high O content render it favorable for constructing O-rich OAPCs with massive micro-mesopores and increased bulk densities [40]. Moreover, their intrinsic 3D interconnected frame minimizes matter diffusion resistance by reducing the tortuosity of transport pathways, increasing the accessibility and interaction between ions/molecules and active sites. Wu *et al.* [41] adopted $C_6H_{11}KO_7$ self-activation and thiourea self-doping craft, acquiring mesopore-dominated N/S co-doped hierarchical porous carbons (HPCs) (NSHPC) with a high S_{BET} of 920.0 m^2/g and plentiful mesopores (Figs. 2c-f). By using bacterial celluloses, Feng *et al.* [42] introduced extra microporosity into $C_6H_{11}KO_7$-based OAPCs, gaining a high specific capacitance of 437 F/g at 0.5 A/g (Fig. 2g).

2.1.3. Potassium acetate (CH_3COOK)

CH_3COOK, recognized as a non-corrosive and eco-friendly organic salt, holds industrial potential for the scalable production

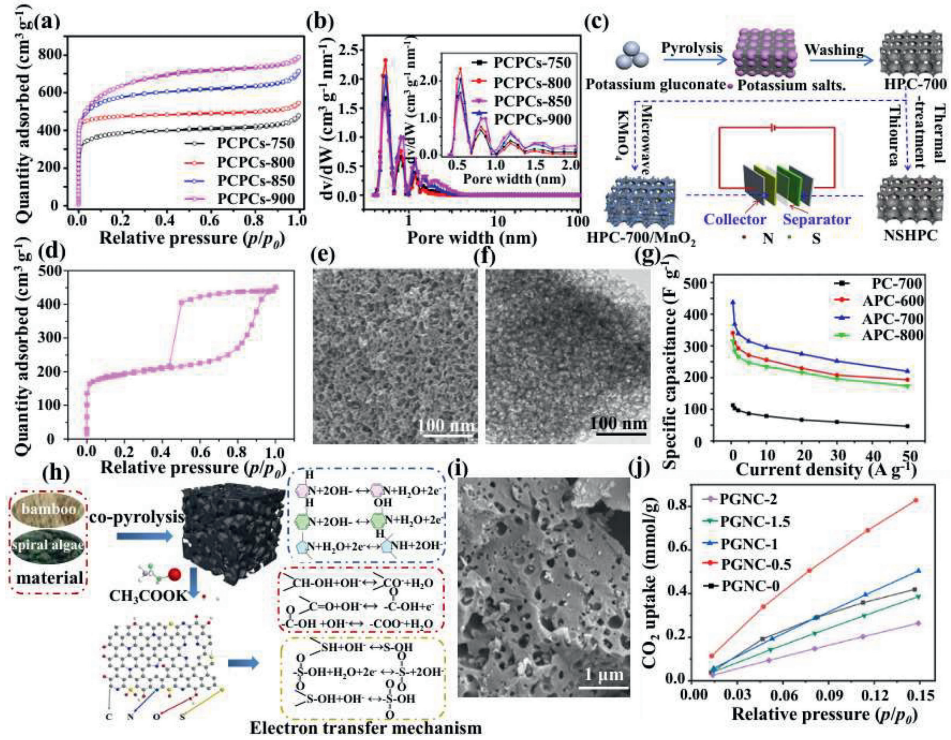


Fig. 2. (a) N_2 adsorption-desorption curves and (b) pore size distribution of PCPCs-*x*. Reprinted with permission [37]. Copyright 2017, Elsevier. (c) Schematic illustration of the fabrication process of NSHPC. (d) N_2 adsorption-desorption isotherms, (e) SEM and (f) TEM images of NSHPC. Reprinted with permission [41]. Copyright 2021, Elsevier. (g) Specific capacitance of PC-700 and APC-X. Reprinted with permission [42]. Copyright 2021, Elsevier. (h) The fabrication route and (i) SEM images of NOS-AC. Reprinted with permission [46]. Copyright 2024, Elsevier. (j) Diluted CO_2 uptake isotherms of PGNC at 25 °C. Reprinted with permission [47]. Copyright 2021, Elsevier.

of OAPCs. While it's monofunctional -COOH and low carbon content often induces limited S_{BET} and underdeveloped porosity, it proves distinct activation efficacy ascribed to its structural analogy to K_2CO_3. Reports reveal that CH_3COOK decomposition initiates at 500 °C, forming $K_2C_2O_4$ intermediate phase, which then undergoes decarbonylation to generate K_2CO_3 (Eq. 3) [43]. This multistage pyrolysis pathway induces intensive etching of carbon matrices by redox reactions between alkaline species (K_2CO_3/K_2O) and carbon skeletons (Eqs. S2-S5) [44], producing OAPCs with tunable micro-mesopore ratios and enhanced structural stability.

$$CH_3COOK \rightarrow K_2CO_3 + CO_2 \quad (3)$$

CH_3COOK-based OAPCs often have rich micropores [45]. Yue *et al.* [46] designed novel N/O/S co-doping PCs (NOS-AC) using CH_3COOK activating spiral algae or bamboo (Fig. 2h). Based on the gas exfoliation effect, NOS-AC delivered superior hierarchical porous structures with a high S_{BET} of 1285.2 m^2/g and large V_{pore} of 0.57 m^3/g (Fig. 2i). Also, Hui *et al.* [47] fabricated an N/O-rich irregular block structural ultramicropore carbon by CH_3COOK co-activating urea-d-glucose. When utilized for the capture of CO_2, it respectively achieved a high adsorption capacity of 1.38 mmol/g and 0.57 mmol/g at 0.15 and 0.05 bar (0 °C) (Fig. 2j).

2.1.4. Other organic potassium salt

Another potassium salts, *e.g.*, potassium tartrate ($C_4H_4K_2O_6$), potassium alginate ($C_{12}H_{16}K_2O_{13}$) and EDTA-2K ($C_{10}H_{17}KN_2O_8$), have manifested nailing efficacy in the synthesis of OAPCs [48–50]. Pyrolysis analysis uncovers that most potassium salts undergo a similar activation pathway, which is first conversion into K_2CO_3, followed by a violent activation reaction (Eqs. S2-S5), thus in turn forming developed pore structures. As a special case, the multi-level porosity of EDTA-2K-derived OAPCs is from the gas etching effect (*in-situ* released H_2O, CO, CO_2 and NO_x) and group self-intercalation effect (-COOK) [48]. Notably, potassium salts have clear advantages in activation ability and template removal, and their activity is higher than but not limited to sodium, magnesium, calcium, zinc and ammonium-based organic salts.

2.2. Organic sodium salt

2.2.1. Ethylenediaminetetraacetic acid disodium ($C_{10}H_{14}N_2Na_2O_8$)

EDTA-2Na, an economical chelating agent, is suited to develop N-rich OAPCs [51]. Research highlights that EDTA-2Na-derived OAPCs are superior candidates due to the unique micro-mesopore structures, N self-doping feature and excellent hydrophilicity [52]. Related to heavy metal salts (*e.g.*, $ZnCl_2$) and rigid templates (*e.g.*, SiO_2), it has the unique gas etching effect that can form controllable hierarchical porosity by releasing H_2O, CO, CO_2 and NO_x during pyrolysis [52]. Also, *in situ* -COONa further betters the activation ability by group self-intercalation effect, inducing improved porosity [53].

Tan *et al.* [54] built a series of OAPCs by EDTA-2Na self-activation (Fig. 3a). The optimal PC-750 achieved a high S_{BET} of 976.9 m^2/g, large V_{meso}/V_{pore} of 24.2 % and 4.86 % high N-doping, thus inducing a high desalting capacity of 8.02 mg/g in 25 mg/L NaCl (Figs. 3b and c). By adopting EDTA-2Na activating taraxacum mongolicum, Chen *et al.* [52] designed biomass-derived OAPCs with legible meso-macropore structures, plentiful active sites and higher N content of 5.99 %. When utilized for EF degradation of methylene blue (MB), it realized rapid electrolyte penetration and ion transport rate. Through transition metal-EDTA-2Na one-step complexation and self-template strategy, Song *et al.* [55] designed one Fe/Mn-NHPC with a high S_{BET} of 939.1 m^2/g and impressive V_{meso}/V_{pore} of 68 % (Figs. 3d and e).

2.2.2. Sodium citrate ($C_6H_5Na_3O_7$)

$C_6H_5Na_3O_7$ has been used for high-yield synthesis of OAPCs. However, they are mainly adopted for the energy and sensing

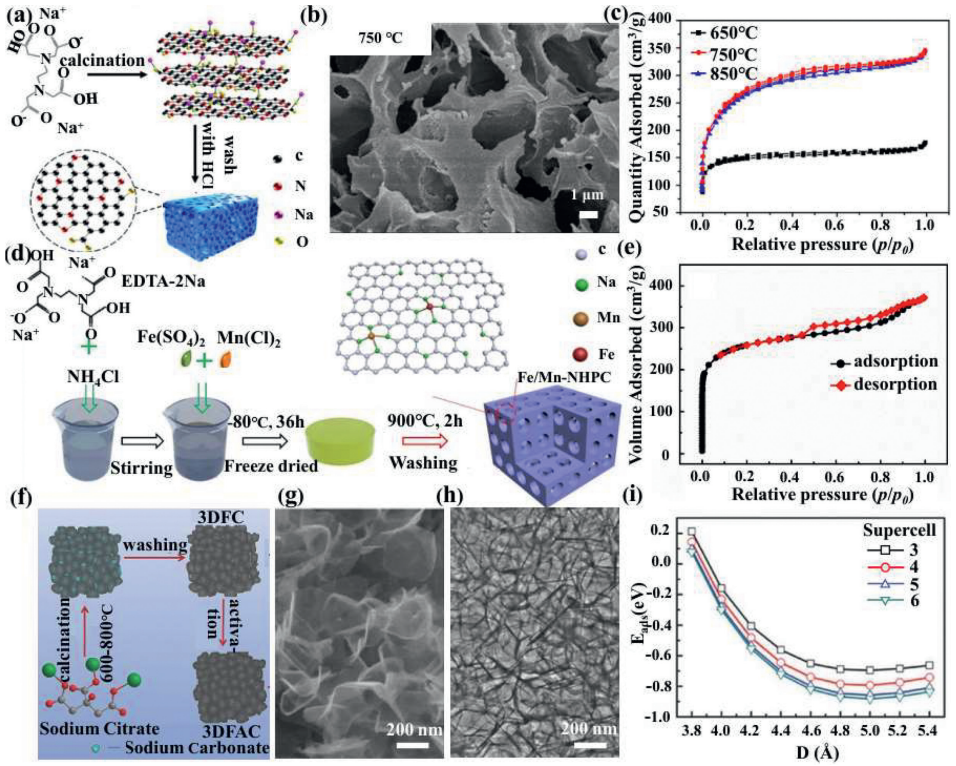


Fig. 3. (a) Schematic of the fabrication process of PC-X and the CDI tests. (b) SEM images of PC-750. (c) N_2 adsorption-desorption isotherms of PC-X. Reprinted with permission [54]. Copyright 2019, Elsevier. (d) Schematic of the preparation process and (e) N_2 adsorption-desorption isotherms of Fe/Mn–NIHPC. Reprinted with permission [55]. Copyright 2022, Elsevier. (f) Schematic of the fabrication process of 3D framework carbon (3DFC). (g) SEM and (h) TEM images of 3DFAC. (i) Distance dependence of adsorption energy between Na atom and graphene layers. Reprinted with permission [28]. Copyright 2017, Wiley.

fields. It features copious -COOH and -OH, favoring the precursor crosslinking and O self-doping. Mass spectrometry coupled with thermogravimetric reveals a dual-stage activation mechanism: (i) Initial decomposition below 650 °C to generate Na_2CO_3 (Eq. 4); (ii) Na_2CO_3-mediated redox reaction and gas etching effect (Eqs. S6-S9 in Supporting information) [28]. Notably, the released Na vapors, CO_2 and CO favor effective pore expansion, promoting the development of regular mesoporous structures with moderate S_{BET} [56].

$$C_6H_5Na_3O_7 \rightarrow 3Na_2CO_3 + CO_2 + H_2O \quad (4)$$

$C_6H_5Na_3O_7$-based OAPCs normally exhibit limited V_{pore} and narrow pore size distribution, which shackles the synergistic effect between tertiary pores. Although adding the pyrolysis temperature can improve the porosity, it may lead to a lower carbon yield [57]. Moreover, due to the nature of sodium, the obtained OAPCs often have lower conductivity than that of potassium salts. Yang *et al.* [28] fabricated well-designed 3D framework carbons (3DFC) by direct $C_6H_5Na_3O_7$ pyrolysis (Figs. 3f-h). DFT calculations uncovered that its large interlayer spacing and curvature structure accelerated the insertion and extraction of Na^+ (Fig. 3i). Thus, 3DFC displayed a high reversible capacity and splendid cycling stability. The diversity in the pore-forming mechanisms between potassium and sodium salts present a promising research area for exploiting OAPCs with wonderful S_{BET} and porosity.

2.2.3. Sodium lignosulfonate ($C_{20}H_{24}Na_2O_{10}S_2$)

Lignosulfonate (SLS), as a by-product from the sulfite pulping, converting to OAPCs is an alternative potential path [58]. SLS is a promising self-activator for preparing mesoporous-dominated OAPCs due to its natural structure, high carbon content and rich N/O/S elements. However, SLS-based OAPCs often have a low S_{BET}, limited V_{micro} and poor graphitization degree [59,60]. This is owing to the inadequate activation and pyrolysis ability of the produced Na_2SO_4 during pyrolysis [61]. Their low S_{BET} translates to fewer active sites, thus reducing the material capability.

To address the above obstacles, Shi *et al.* [62] developed a GO-mediated activation-self-activation craft using $K_2C_2O_4$-SLS bi-activators (Fig. S2a in Supporting information), designing mesopore-dominated N-doped HPCs (ENHPC) with a high S_{BET} of 1795.5 m^2/g, improved V_{micro}/V_{pore} of 23 % and enhanced conductivity (Figs. S2b-d in Supporting information). When assembled for Ni(II) desalination, ENHPC respectively acquired a high salt removal capacity and rate of 17.86 mg/g and 0.99 mg/g/min in 10 mg/L Ni(II). To integrate high yield-high performance, Shi *et al.* [63] designed SLS-$KHCO_3$-KNO_3 systems, yielding defect-rich N/S Co-doped HPCs ($NSHPC_{SKK}$) (Fig. S2e in Supporting information). Its extensive defect structures were certified by *ex-situ* Raman (Fig. S2g in Supporting information), with further revelation of N/S co-doping at defect sites by XPS. DFT analysis determined that N/S co-doped defect structures had strong adsorption effects on Na atoms. Therefore, it depicted a rapid average desalting rate of 12.1 mg g^{-1} min^{-1}.

2.2.4. Sodium glutamate ($C_5H_8NNaO_4$)

Gourmet powder, *e.g.*, $C_5H_8NNaO_4$, is an easily accessible organic salt rich in N, making it suitable for fabricating N-doped OAPCs [64]. Activation mechanism involves the transformation of $C_5H_8NNaO_4$ into $C_5H_6NO_3$-Na through decomposition and gasification. Whereafter, it decomposes to form Na_2CO_3 at 550-650 °C, followed by the same activation mechanism as Na_2CO_3 (Eqs. S6-S9) [65]. $C_5H_8NNaO_4$-based OAPCs normally have unique hierarchical porous structures that favor rapid ion transfer. Meanwhile, the N self-doped characteristic introduces the extra pseudocapacitance effect, strengthening the specific capacitance.

By $C_5H_8NNaO_4$-NaCl co-activation, Qian *et al.* [66] prepared a series of $C_5H_8NNaO_4$-derived N-doped HPCs under different pyrolysis temperatures and times. The optimal SMC-800-2 exhibited a large S_{BET} of 1007.62 m^2/g, superior V_{pore} of 0.56 cm^3/g and high N doping level (Fig. S2f in Supporting information). Similarly, Sun *et al.* [67] also manufactured 3D N-doped OAPCs (3D-NPC) by $C_5H_8NNaO_4$-NaCl co-carbonization (Fig. S2h in Supporting information). Due to high N content of 4.93 % and large S_{BET} of 1481.0 m^2/g, 3D-NPC with an interconnected hierarchical porous structure displayed an excellent desalting capacity of 19.4 mg/g and superior cycle stability (Fig. S2i in Supporting information).

2.3. Organic zinc salt

Organic zinc salts include zinc gluconate ($C_{12}H_{22}O_{14}Zn$), zinc acetate ($Zn(CH_3COO)_2$), $EDTANa_2Zn$ ($C_{10}H_{14}N_2O_8Na_2Zn$), *etc.* [68,69]. For $C_{12}H_{22}O_{14}Zn$, it initiates with carbothermal reduction, yielding $ZnCO_3$ that self-integrates into the carbon matrix (Eq. S10 in Supporting information). As temperature increases, the residual $ZnCO_3$ decomposes to ZnO, which chemically interacts with the carbon (Eq. S11 in Supporting information). When temperatures > 900 °C, $ZnCO_3$ races reductive reactions with carbon to produce metallic Zn and Zn vapors. These reactions induce intense surface etching, generating micropore-dominated hierarchical porous structures (Eqs. S12 and 13 in Supporting information) [69]. Similarly, $Zn(CH_3COO)_2$ thermally decomposes into ZnO and other gases, which synergistically engineer mesopore-rich carbon networks *via* dual mechanisms: (i) ZnO for pore confinement and (ii) *in situ* gas etching effect for pore interconnection enhancement.

$EDTANa_2Zn$ delivers distinct activation pathways, primarily through its thermal decomposition under elevated temperatures to produce ZnO and Na_2CO_3 (Eq. 5) [70]. During pyrolysis, organic components can carbonize to form a carbon matrix, which then engages in carbothermal reduction with ZnO, thus releasing gases and Zn vapors. The gas etching effect can adjust porosity and refine pore size distribution. Moreover, its intrinsic N species can be incorporated into the carbon lattice *via in-situ* doping, thereby introducing extra active sites and bettering surface hydrophilicity. This favors matter transport and augments material performance.

$$C_{10}H_{14}N_2O_8Na_2Zn \rightarrow ZnO + Na_2CO_3 + CO_2 + H_2O \quad (5)$$

Through directly pyrolyzing EDTA-2K at 800 °C, Shi *et al.* [48] fabricated an N-doped HPC (NC-800). As expected, it acquired a prominent S_{BET} of 2703.0 m^2/g, large V_{pore} of 1.7 cm^3/g and doped carbonyl and nitrogen groups (Figs. 4a and b). When taken for the adsorption of sulfamethoxazole (SMX), it realized an almost 99.5 % removal rate. Gao *et al.* [70] designed rich-defective OAPCs *via* EDTA-3K-$Zn(CH_3COO)_2$ co-activation (Fig. 4c). Herein, EDTA-3K produced micropores, while Zn $(CH_3COO)_2$ generated meso-macropores, thus building hierarchical porous structures (Fig. 4e). This scheme accelerates electrolyte penetration and ion diffusion pathways. Moreover, O-containing groups and intrinsic defects in OAPCs promoted charge transfer, expanded the graphite layer spacing and constructed more accessible active sites (Fig. 4d).

2.4. Organic magnesium salt

Organic magnesium salts are also excellent activators owing to their sustainability and high pore formation ability. Magnesium salts involve magnesium citrate ($C_{12}H_{10}Mg_3O_{14}$), magnesium acetate ($Mg(CH_3COO)_2$) and magnesium gluconate ($C_{12}H_{22}MgO_{14}$) [71,72]. For $C_{12}H_{10}Mg_3O_{14}$, the molten-phase behavior at high temperatures facilitates the graphitic domain delamination and pore structure reconstruction. Meanwhile, *in situ* formed $MgCO_3$ can be embedded within the carbon framework. Subsequent thermal dissociation of residual $MgCO_3$ yields MgO and CO_2, the latter can improve surface porosity by gas etching effect [72]. The coordinated templating-etching strategy produces carbon networks with multiscale porosity spanning micro- and mesopores, exhibiting optimized matter transport kinetics. Similar activation principles govern $Mg(CH_3COO)_2$-based OAPCs, where staged decomposition products co-modulate pore structures [71].

Nie *et al.* [73] prepared unique HPCs by the $C_{12}H_{10}Mg_3O_{14}$ self-activation strategy (Fig. 4f). Research revealed that HPC-800 exhibited a high S_{BET} of 1636.0 m^2/g, prominent V_{pore} of 2.30 cm^3/g, ultrahigh V_{meso}/V_{pore} of 95.5 % and plentiful negative surface charges (Fig. 4g). Further CDI tests indicated that it had excellent ion-selective and rapid dynamic rate (Fig. 4h). 3D interconnected hierarchical structures are much more conducive to the diffusion, migration and adsorption of matters. Shi *et al.* [74] prepared 3D N-doped HPCs *via* a carbonization-activation method (Fig. 4i). In the carbonization step, the 3D interconnected skeleton was built by $C_{12}H_{22}MgO_{14}$-NaCl co-pyrolysis, where NaCl and pyrolysis-generated MgO played a crucial role. During the activation step, $KHCO_3$ and urea expanded the micropores and introduced massive N elements. Eventually, $C_{12}H_{10}Mg_3O_{14}$-derived N-doped OAPCs (MNC) delivered a high S_{BET} of 2423.0 cm^2/g and large V_{pore} of 1.24 cm^3/g. When taken for CO_2 capture, it gained a high adsorption capacity of 4.22 mmol/g at 25 °C and 1 bar.

2.5. Organic calcium salt

Organic calcium salts can often pyrolyze and decompose before self-activation, *in situ* generating $CaCO_3$, and then producing CaO and massive gases, thus gradually converting organic components into OAPCs. For instance, calcium acetate ($Ca(CH_3COO)_2$) can pyrolyze and generate $CaCO_3$, which further yields CaO to interact with carbon and produce CO_2 to etch the carbon skeleton, thereby forming copious porosity (Eqs. S14 and S15 in Supporting information) [75]. Another typical salt is $EDTANa_2Ca$ ($C_{10}H_{12}CaN_2Na_2O_8$). It can first pyrolyze to form CaO and Na_2CO_3 as well as CO_2 and H_2O vapors (Eq. S16 in Supporting information), producing strong internal activation of the carbon skeleton and promoting the pore structure development, thus forming micro-mesopores. According to the dual template effect and gas etching effect, $EDTANa_2Ca$-derived OAPCs often possess hierarchical porous structures and a more reasonable pore size distribution. Moreover, its pyrolysis can also *in situ* introduce N elements into OAPCs, which can greatly improve their surface wettability and conductivity, thus favoring the migration, diffusion and adsorption of matters and enhancing mass/charge transfer.

Sheng *et al.* [76] designed N-doped porous carbon nanosheets (NPC-Ca_xK_y) by the synergy effect of $Ca(CH_3COO)_2$-CH_3COOK-melamine (Fig. S3a in Supporting information). Due to the *in situ* generated $CaCO_3/K_2CO_3$ and the foaming effect of melamine, the optimal NPC-$Ca_{1.5}K_3$ showed clear hierarchical porosity with a high S_{BET} of 2546.6 m^2/g, large V_{pore} of 1.32 cm^3/g and 2.47 % high N doping (Fig. S3b in Supporting information). By direct pyrolysis of $EDTANa_2Ca$, Hu *et al.* [77] gained a series of NHPCs. Herein, Na_2CO_3 templates promoted the production of meso-macropores, thus inducing the formation of well-developed hierarchical porosity. Ultimately, NHPC-850 acquired a high S_{BET} of 2015.0 m^2/g and large V_{pore} of 1.74 cm^3/g.

Zhang *et al.* [78] constructed biomass-derived OAPCs by $Ca_3(C_6H_5O_7)_2$ activating biomass pyrolysis vapors (Figs. S3c and d in Supporting information). The influences of precursor preparation and pyrolysis temperature, and heating rate on the yield of biomass pyrolysis products, composition of light bio-oil and structure of OAPCs were explored. Research indicated that its plentiful O-containing functional groups induced the gas etching effect, which combined with the CaO template effect, realized the micropore generation. The optimal material gained a high S_{BET} of 1703.0

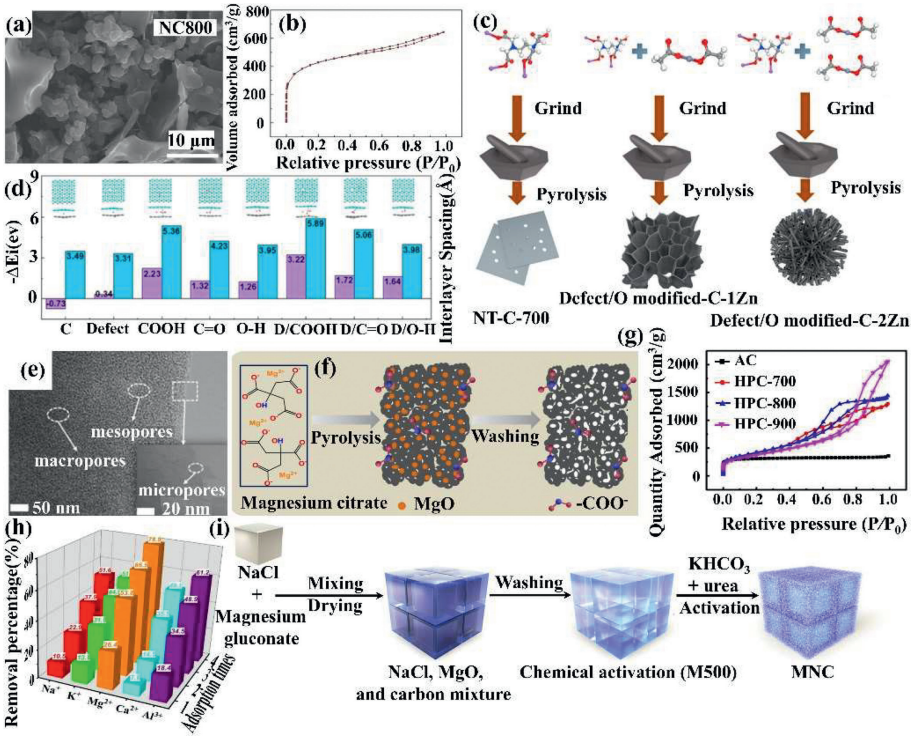


Fig. 4. (a) SEM images and (b) N_2 adsorption-desorption isotherms of NC800. Reprinted with permission [48]. Copyright 2020, Elsevier. (c) Schematic illustration of the preparation process and (e) TEM images of Defect/O modified-C. (d) The interlayer space and intercalated energy of K^+ on diverse GO configurations of pure carbon. Reprinted with permission [70]. Copyright 2021, Elsevier. (f) Schematic illustration of the preparation of HPC-700. (g) N_2 adsorption-desorption isotherms of AC and HPC-X. (h) Cations' selective adsorption ability of HPC-700. Reprinted with permission [73]. Copyright 2022, Elsevier. (i) Schematic illustration of the preparation process of MNCs. Reprinted with permission [74]. Copyright 2025, Elsevier.

m^2/g and splendid V_{meso}/V_{pore} of 24.17 %. Thus, it realized a superior H_2 adsorption capacity of 170.1 cm^3/g (1.53 wt%) at 77 K at 25 °C.

2.6. Organic ammonium salt

Organic ammonium salts are a kind of wonderful activator due to their sustainability and outstanding activation effects. However, there is relatively little research. Ammonium salts mainly include ammonium citrate ($C_6H_5O_7(NH_4)_3$), ferric citrate ($C_6H_5FeO_7$) and ferric ammonium citrate ($(NH_4)_xFe_y(C_6H_4O_7)_z$). For $C_6H_5O_7(NH_4)_3$, the generated volatile compounds can be embedded into the carbon frame during pyrolysis, and then decompose to produce NH_3 and CO_2 *via* the decarboxylation reaction. This behavior constitutes a strong gas etching effect on the precursor, thus forming copious porosity. This improvement induced a decrease in matter diffusion/charge transfer resistance, thereby improving the overall performance and enhancing the dynamic [79].

Zhu *et al.* [80] adopted $(NH_4)_xFe_y(C_6H_4O_7)_z$ as C/Fe sources and GO as structure-directing agents, building a C-G/AFC with interconnected structures (Fig. S3e in Supporting information). Viewing the synergy effect of $(NH_4)_xFe_y(C_6H_4O_7)_z$ and GO, C-G/AFC achieved a medium S_{BET} of 113.4 m^2/g and 1.73 % high N doping (Fig. S3f in Supporting information). In another research, Cheng *et al.* [81] took kiwifruit as precursors and $(NH_4)_xFe_y(C_6H_4O_7)_z$ as activators, gaining biomass-based OAPCs (Fig. S3g in Supporting information). Here, Fe and NH_3 generated form $(NH_4)_xFe_y(C_6H_4O_7)_z$ improve the graphitization degree of OAPCs and construct porous framework structures, respectively.

It is vital to reveal the effect of organic ammonium salt on the morphology of OAPCs. Qiang *et al.* [82] adopted $C_6H_5O_7(NH_4)_3$-$C_6H_5K_3O_7$ co-activation craft to fabricate crimped porous carbon nanosheets (Fig. S3h in Supporting information). Compared with the S_{BET} of 1159.2 cm^2/g, V_{micro} of 0.48 cm^3/g and V_{meso}/V_{pore} of 27.3 % for single $C_6H_5K_3O_7$ derived OAPCs, its S_{BET}, V_{micro} and V_{micro}/V_{pore} were 1668.3 cm^2/g, 0.52 cm^3/g and 42.2 %, respectively. Next, by introducing urea co-pyrolysis, the final $HNHPC_{PUA}$ had up to 3280.2 m^2/g for S_{BET}, 2.49 cm^3/g for V_{pore} and 6.4 % for N doping (Fig. S3i in Supporting information). These results revealed that both urea and $C_6H_5O_7(NH_4)_3$ can tune the pore structure and surface chemistry properties of OAPCs, and $C_6H_5O_7(NH_4)_3$ mainly adjusted the pore size.

2.7. Mechanism identification

High-performance OAPCs should own the following merits, such as high accessible S_{BET}, appropriate pore size distribution, superior conductivity, prominent stability and high carbon yield. The physicochemical properties and pore structure indices of diverse OAPCs were summarized in Fig. 5 and Table S1 (Supporting information). The evaluation indicators involved activation ability, S_{BET}, pore size distribution, activator types, surface charges, graphitization degree and element doping. It can be seen that single organic salt-based OAPCs are hard to integrate the above advantages. Sodium salts often have weak activation ability, thus inducing a medium S_{BET}. Due to the size effect of Na_2CO_3 and *in situ* N-doping of sodium salts, its derived OAPCs are mainly mesoporous and own certain N-doping. Zinc salts-derived OAPCs indicated similar structural characteristics and chemical properties to sodium salts. However, because it releases Zn vapor during pyrolysis, its derived OAPCs also have certain micropores. Notably, viewing calcium salts and ammonium salts has extra gas etching effects, S_{BET} of their derived OAPCs can be further improved. Although manesium salts delivered a strong activation ability, its derived OAPCs are also mainly mesoporous. Notably, among the various salts, potassium salts are still optimal and it is vital to identify

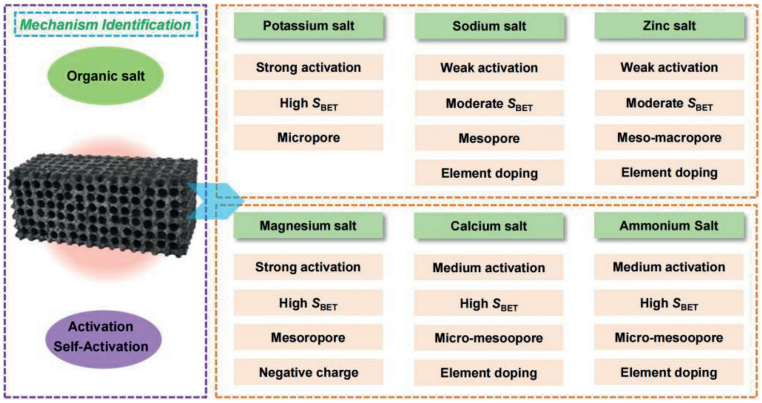


Fig. 5. Physicochemical properties of different sustainable OAPCs.

the other salts that as auxiliary activators, may have a better effect. Future exploration of potassium-based OAPCs involves the following three aspects: (1) Construct bi- or multi-activator systems that utilize the synergistic effects of diverse metal activators to build OAPCs with tertiary pore structures and high yield; (2) Construct foaming agent-assisted activation systems (*e.g.*, urea, melamine and thiourea), fabricate high N/S-doped OAPCs with ultrahigh S_{BET} and microporous ratio; (3) Construct O-rich activation systems, prepare OAPCs with ample surface charges to reinforce their application selectivity.

3. Dimensional control of OAPCs from 0D to 3D

Compared with biomass, polymer and template-constructed precursors, the structure of OAPCs is greatly limited by the molecular arrangements and chemical nature of organic salts. So far, massive work has been devoted to optimizing their structure from 0D to 3D, *e.g.*, carefully choosing organic salts, precisely controlling synthesis conditions and innovatively exploiting new fabrication processes [83]. These efforts aim to surmount the limitations of organic salts and develop OAPCs with tailored structures to adapt to diverse environmental applications.

3.1. Zero-dimensional architecture

0D PCs, *e.g.*, carbon nanoparticles, refer to PCs that are confined to the nanoscale in all three dimensions, which mainly exist in the form of spherical, cubic and prismatic [84]. 0D PCs hold several distinctive characteristics. It can serve as both active materials or carriers, achieving high exposure of the accessible active sites of active materials [85]. Due to the regular geometry, small structural size and tunable pore structure, OD PCs also own an excellent S_{BET} and improved hydrophilicity, thereby bettering the interaction between ions/molecules and target OAPCs [86,87]. Further, their high tap density favors high volumetric performance. Their typical synthesis methods include the hydrothermal method, multi-stage pyrolysis method, spray drying method, *etc.*

Based on the spray drying and carbonization-activation craft, Liu *et al.* [58] designed hierarchical porous carbon spheres (HPCS) from SLS (Fig. 6a). Research disclosed that the spray drying played a decisive role in the 0D precursor formation. As expected, HPCS delivered tertiary structures, ultrahigh S_{BET} of 3402 m^2/g and superior V_{pore} of 2.46 cm^3/g. When adopted for CH_2Cl_2 capture, HPCS acquired a high adsorption capacity of 181.0 mg/g (Fig. 6b). Mechanism research revealed that meso-macropores offer rapid transport channels, and micropores provide massive adsorption sites. Pang *et al.* [88] exploited a two-stage pyrolysis craft, gaining a series of SLS-derived HPCSs with clear tertiary structures (Fig. 6c). Here, the low-temperature carbonization step was mainly used for the finalization of spherical precursors, while the high-temperature pyrolysis was utilized to obtain multi-level porosity. By temperature regulation, HPCS-900 acquired a high S_{BET} of 1939.0 m^2/g and large V_{pore} of 1.42 cm^3/g (Fig. 6d).

Integrating highly developed pore structures in 0D OAPCs is vital to accelerate the matter diffusion and enhance the material ability. Qiang *et al.* [82] designed $C_6H_5O_7(NH_4)_3$-urea-co-assisted $C_6H_5K_3O_7$ crafts to gain high N-doped hierarchical porous carbon nanogranules (HNHPC) (Figs. 6e and f). Viewing the synergistic effect of the self-activation effect ($C_6H_5O_7(NH_4)_3$-$C_6H_5K_3O_7$) and foaming effect (urea), it realized an ultrahigh S_{BET} of 3280.2 m^2/g, large V_{meso}/V_{pore} of 57.83 % and 6.40 % high N-doping level (Figs. 6g and h). Research showed that $C_6H_5O_7(NH_4)_3$ took a decisive role in the formation of HPCS, while urea played a leading role in regulating the N content and the particle size.

3.2. One-dimensional architecture

1D PCs, *e.g.*, carbon nanowires or carbon nanotubes (CNTs), have multiple advantages such as high S_{BET} and controllable pore structure, efficient mass transfer and superior structural stability [89–92]. Typically, the unique hollow configuration and superior charge transport properties of CNTs have driven wide research interest [93]. Nonetheless, scaling up CNTs faces huge challenges, *e.g.*, costly precursor expenses and intricate synthesis processes needing precise control [94]. Despite these advantages, the current research indicates that exploited organic salt-derived 1D OAPCs is still very limited. In a case, to seek 1D frameworks to inhibit the inactivation of Se, Chen *et al.* [95] manufactured a Se-hierarchical porous carbon fiber (Se-HPCF) by electrostatic spinning craft taking SLS as precursors/self-activators (Fig. 6i). As a result, Se-HPCF with 1D hierarchical porous structures and copious accessible S_{BET} effectively alleviated the Se inactivation (Fig. 6j). Based on $C_6H_5K_3O_7$/polyacrylonitrile (PAN), Zhang *et al.* [96] constructed a 1D nanoscale carbon fiber membrane (CFM) by the same strategy (Fig. 6k). The optimal CFM gained a medium S_{BET} of 347.8 m^2/g and copious porosity.

3.3. Two-dimensional architecture

2D PCs, *e.g.*, carbon nanosheets, often have a thin thickness on the nanometer scale along with a relatively large aspect ratio and highly exposed S_{BET}. The structure confers many advantages, *e.g.*, short matter diffusion channels and abundant interfacial contact area for migration [97,98]. There is a consensus that graphene is a well-known 2D PC, which is the world's thinnest, strongest and most conductive material [99]. The orthodox preparation methods

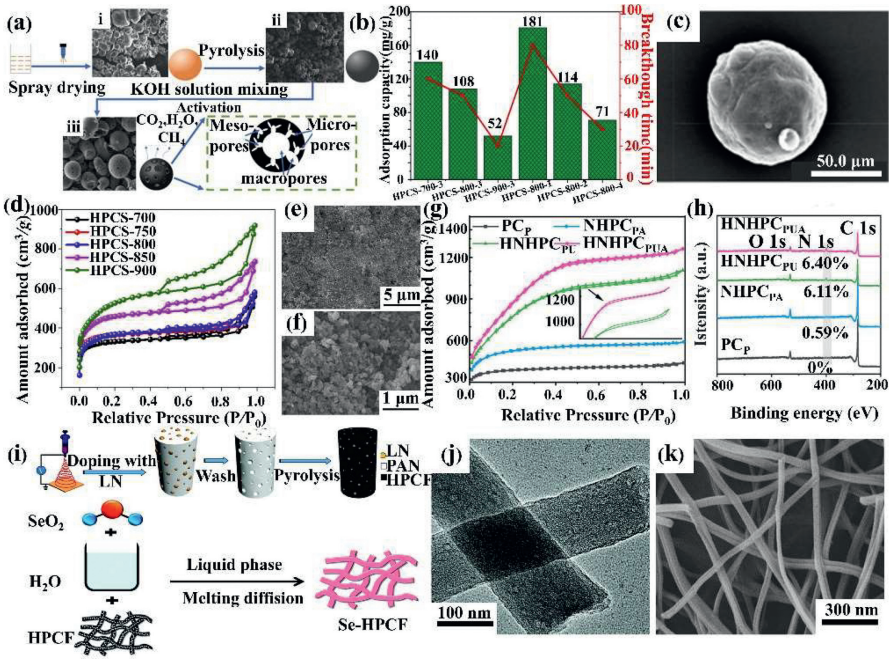


Fig. 6. (a) Schematic illustration of the preparation process of HPCS-X-Y (inset: SEM images). (b) CH_2Cl_2 adsorption capacity and time of HPCS-X-Y. Reprinted with permission [58]. Copyright 2022, Elsevier. (c) SEM images of HPCS-900. (d) N_2 adsorption-desorption isotherms of HPCS-X. Reprinted with permission [88]. Copyright 2018, Elsevier. (e, f) SEM images of $HNPC_{PA}$. (g) N_2 adsorption-desorption isotherms and (h) XPS spectra of diverse OAPCs. Reprinted with permission [89]. Copyright 2023, Elsevier. (i) Scheme of the fabrication process and (j) TEM images of Se-HPCF. Reprinted with permission [95]. Copyright 2020, RSC. (k) SEM images of 1D CFM. Reprinted with permission [96]. Copyright 2022, MDPI.

include the mechanical exfoliation, solution exfoliation and Hummers method [100]. However, these crafts face considerable limitations, *e.g.*, easy stacking, severe oxidation degree and high production cost [101,102]. In this condition, leveraging organic salts for fabricating 2D OAPCs provides a potential proposal. This strategy reduces reliance on costly raw materials, increases structural control precision and streamlines the preparation craft, enhancing the production feasibility for 2D OAPCs.

Single organic salts can be directly pyrolyzed to obtain 2D OAPCs. By directly pyrolizing $C_{12}H_{22}Ca_3O_{14}$, Zhang *et al.* [103] prepared a carbon nanosheet with a thickness of 29 nm. SEM and TEM disclosed that the thickness can be controlled within a range of 20-30 nm by varying the pyrolysis temperatures (Figs. S4a-j in Supporting information). XRD and BET showed that the nailing carbon frame was mainly from *in situ*-generated $CaCO_3$, CaO and CO_2. Based on the *in situ* self-activation and KOH activation, $C_6H_{11}KO_7$-based 2D porous carbon nanosheet (2D PCNS) with a superior S_{BET} of 2793.5 m^2/g and splendid V_{pore} of 1.67 cm^3/g was fabricated (Fig. S4k in Supporting information) [104]. When utilized for the capture of MB, it acquired a high adsorption capacity of 688.76 mg/g. Besides, Luo *et al.* [105] prepared a PCN by a rapid EDTA-4Na self-activation strategy (Figs. S4l-n in Supporting information).

Achieving universal preparation and further pore expansion of 2D OAPCs is crucial. Hou *et al.* [106] exploited N/O co-doped PCNs (NOPC) based on the g-C_3N_4-$C_6H_5K_3O_7$ co-activation craft (Fig. S4o in Supporting information). $C_6H_5K_3O_7$ here served as precursors/self-activators, and g-C_3N_4 was adopted to adjust the morphology, porosity and elemental composition of OAPCs. As a result, the optimal NOPC delivered an ultrahigh S_{BET} of 2557 m^2/g, excellent V_{pore} of 1.6 cm^3/g and 3.38 % high N content. Wu *et al.* [29] prepared sodium humate-based PCNS *via* the urea-$C_6H_5K_3O_7$ co-activation strategy (Fig. S4p in Supporting information). By case comparison, we found that urea and g-C_3N_4 had the same pore formation effect, which was mainly due to their unique gas exfoliation effect regulating the morphology of OAPCs and accelerating the formation of sheet layers.

3.4. Three-dimensional architecture

Although 2D PCs possess distinctive advantages, they normally suffer from the drawbacks of easy-to-layer stacking, thus reducing exposed accessible S_{BET} and hindering internal matter migration [107,108]. In contrast, 3D PCs fabricated from low-dimensional subunits preserve the intrinsic merits of individual nanosheets while introducing emergent properties [109]. For instance, such 3D architectures manifest superior structural robustness compared with their 2D counterparts, enabling better tolerance to mechanical stress during usage [110]. Besides, their interconnected porous networks favor directional matter flux and establish seamless conductive/transport pathways [111]. Therefore, engineering 3D OAPCs with hierarchical porosity, improved hydrophilicity and enhanced conductivity is a critical objective.

Sun *et al.* [49] exploited 3D interconnected PCs (IPCs) by facile $C_{12}H_{16}K_2O_{13}$ self-activation (Fig. S5a in Supporting information). The optimized IPC-800 showed an S_{BET} of 1145.8 m^2/g and V_{pore} of 0.58 cm^3/g (Figs. S5b-d in Supporting information). To further augment the interconnection degree within carbon skeletons, Wang *et al.* [112] fabricated 3D interconnected NSHPCs using $C_6H_5K_3O_7$ as activators, enzymes as biocatalysts and cottonseed meal as precursors. Herein, cellulase pretreatment greatly reduced the cellulose content in cottonseed meal from 12.5 % to 2.2 % while establishing porous precursor frameworks. Vitally, the enzymolytic process validly added the O content and promoted the activation efficiency of $C_6H_5K_3O_7$. Thus, the resultant CCM-800-2 showed a high S_{BET} of 1528.0 m^2/g, superior disorder degree and 11.3 % high O content (Fig. S5e in Supporting information). This unique 3D structure effectively accelerated the ion migration and adsorption, thereby realizing an obvious performance breakthrough.

Wang *et al.* [23] developed a novel *in-situ* template-assisted self-activation strategy to construct a series of X-NSMHPCs (X = A, M, N) from diverse sulfate ($Al_2(SO_4)_3$/$MgSO_4$/$(NH_4)_2SO_4$) precipitated kraft lignins (X-KLs, X = Al, Mg, NH_4) (Fig. S5f in Supporting information). Related to other X-NSMHPCs, N-NSMHPC presented distinct mesoporous-dominated hierarchical porous structures with high S_{BET} of 622.1 m^2/g and copious N/S doping level (Figs. S5g-i in Supporting information). Research depicted that its distinct tertiary pore structure and massive surface-exposed active sites accelerated electrolyte penetration and promoted ion insertion and extraction. Zhu *et al.* [113] utilized $C_4H_4K_2O_6$ to activate fallen leaves (FL)/chicken feathers (CF)/*Enteromorpha prolifera* (*EP*) to gain three diverse 3D OAPCs (Figs. S5j and k in Supporting information). Compared with the low S_{BET} (256.0 m^2/g) of $C_4H_4K_2O_6$-derived OAPCs, S_{BET} for FL-PCM, CF-PCM and EP-PCM were 1721.0, 1819.0 and 2151.0 m^2/g, respectively.

In summary, the section systematically classifies OAPCs into 0D, 1D, 2D and 3D, each with distinct structural characteristics and application advantages. 0D OAPCs (*e.g.*, nanospheres and particles) have high S_{BET} and uniform pore distribution, enabling efficient adsorption and rapid charge transfer, which are ideal for ion/molecule capture. 1D OAPCs (*e.g.*, nanowires and tubes) offer unique axial channels, optimizing mass transport and mechanical stability, making them more suitable for electrochemical devices and composite reinforcements. 2D OAPCs (*e.g.*, nanosheets) show ultrathin structures with highly exposed active sites, favoring rapid ion diffusion and catalytic reactions. 3D OAPCs (*e.g.*, foams and networks) integrate interconnected pore systems, combining high S_{BET} with superior structural robustness, excelling in applications requiring multi-scale mass transport, such as adsorption and CDI. This dimensional diversity enables OAPCs to address specific environmental issues by tailoring structure-property relationships for targeted applications.

4. Environmental applications

OAPCs, ascribed to the high S_{BET}, tunable pore structure, excellent conductivity and superior chemical stability, have been proven wide application foreground in the environmental fields. OAPCs provide innovative solutions to challenges such as water pollution, gas purification and electromagnetic radiation *via* different mechanisms of adsorption, catalysis and absorption. Their environmental applications are prominently reflected but not limited to the following five domains.

4.1. Adsorption

Adsorption is a phenomenon where gas or liquid molecules are concentrated on the adsorbent surface [114]. Presently, adsorption has been used for the deep treatment and purification of hazardous substances in soil, water and gas. Compared with biodegradation, membrane technology and ozonation with poor longevity, high costs, serious membrane fouling and massive toxic degradation intermediates, adsorption has attracted broad attention owing to its low costs, facile operation, high efficiency and sustainability [115]. Normally, traditional PCs face high costs, process complexity and low carbon yield, whereas OAPCs can avoid the above constraints. The adsorption of pollutants on OAPCs is mainly determined by physical-chemical nature, *e.g.*, S_{BET}, V_{pore}, pore size distribution and chemical composition. The main adsorption mechanisms involve pore filling, electrostatic interaction, hydrogen bonding, π-π interaction *etc.* Table S2 (Supporting information) gives the adsorption capacity and adsorption mechanism of typical OAPCs.

In the solution adsorption aspect, Tan *et al.* [116] adopted the EDTA-2Na self-activation to build PC-650 and PC-750 (Fig. 7a). Thereinto, PC-750 gained a high S_{BET} of 1354.7 m^2/g and large V_{meso}/V_{pore} of 37.5 % (Fig. 7b). As expected, PC-750 achieved a high MB adsorption capacity of 1354.7 mg/g, and its adsorption behavior was coincidental to the Langmuir isotherm model and pseudo-second-order kinetic model. By $C_6H_5K_3O_7$-$C_6H_5FeO_7$ co-activating *EP*, Qin *et al.* [117] fabricated a porous carbon/porous biochar (PC/PB). Viewing their synergistic effect, PC/PB showed unique tertiary pore structures with a high S_{BET} of 1415.0 m^2/g and large V_{pore} of 1.08 cm^3/g (Fig. 7c). Thus, PC/PB gained a superior adsorption capacity of 844 mg/g for SMX, which is higher than that of reported sorbents (Fig. 7d). Research depicted that the high property mainly relied on pore filling, hydrogen bonding, π-π interaction and electrostatic interaction (Fig. 7e).

In the gas adsorption aspect, Singh *et al.* [118] developed N/O-doped biocarbons using $C_6H_5K_3O_7$ activating casein (Fig. 7f). The optimal CPC-3 (m_{casein}:$m_{activator}$ = 1:3) showed a rough morphology with an ultrahigh S_{BET} of 2212.0 m^2/g and plentiful O/N functional groups (Fig. 7g). Thus, it delivered a high CO_2 capture capacity of 25.4 mmol/g (Fig. 7h). By using urea as N sources/foaming agents and $C_{12}H_{22}O_{14}Zn$ as self-activators, Zhu *et al.* [119] prepared N-doped PCs (DT-NPC) (Figs. 7i and k). Notably, Zn evaporation induced copious micropores, while the gas etching effect helped to build tunable meso-macropores and massive N-doping sites (Fig. 7j). Thus, DT-NPC-3 acquired a high SO_2 adsorption capacity of 11.8 mmol/g (25 °C, 1.0 bar). Besides, the selectivity of SO_2/N_2 (0.1/0.9) and SO_2/CO_2 (0.1/0.9) was separately198.7 and 21.5 (Figs. 7l and m).

4.2. Capacitive deionization

CDI is an emerging seawater desalination technique based on electric double-layer capacitors [120]. Related to electrodialysis, reverse osmosis and multi-stage flash, CDI is more competitive to treat low-concentration brine and is energy-saving, no secondary pollution and low cost [121]. In operation, ions in brackish water can be rapidly adsorbed onto electrodes with opposite charges at a low voltage, and they can then be desorbed by the short-circuit [122]. Electrode materials (*e.g.*, PCs and carbon composites) are the CDI core that greatly affect the key indexes of salt adsorption capacity/rate, productivity and cycle stability [120–123]. OAPCs are a splendid selection by virtue of their high S_{BET}, adjustable pore structure, high conductivity and prominent stability. Table S3 (Supporting information) gives the CDI desalination capacity of typical OAPCs.

Shi *et al.* [35] exploited a double organic salt activation craft that utilized Na_2EDTA-$C_6H_5K_3O_7$ to co-activate lotus stems (Fig. S6a in Supporting information). The final 3D N-doped HPC ($3DNHPC_{11}$) achieved a high S_{BET} of 2256.2 m^2/g and large V_{meso}/V_{pore} of 60.0 % (Figs. S6b and c in Supporting information). When taken for CDI desalination, it respectively gained a superior desalting capacity/rate of 22.21 mg/g and 5.56 mg g^{-1} min^{-1} in 500 mg/L NaCl at 1.2 V. The excellent performance was due to unique hierarchical porous structures and massive accessible active sites promoting electrolyte penetration and ion transport (Fig. S6d in Supporting information).

To further accelerate the desalting dynamics, Lu *et al.* [63] designed SLS-$KHCO_3$-KNO_3 co-activation systems and prepared defect-rich N/S co-doped HPCs (NSHPC). Its defective structure was certified by Raman, with further revealing N/S co-doping at defect sites by XPS. DFT analysis disclosed that N/S co-doped defects had a strong adsorption effect on Na atoms. Thus, NSHPC showed a faster desalting rate of 12.1 mg g^{-1} min^{-1}. Qiang *et al.* [89] used $C_6H_5O_7(NH_4)_3$-urea co-assisted $C_6H_5K_3O_7$ activation craft to build nanogranule-like NHPCs with ultrahigh S_{BET} and nailing hydrophilicity (Figs. S6e and f in Supporting information), greatly accelerating the electrolyte penetration, inducing a high salt adsorp-

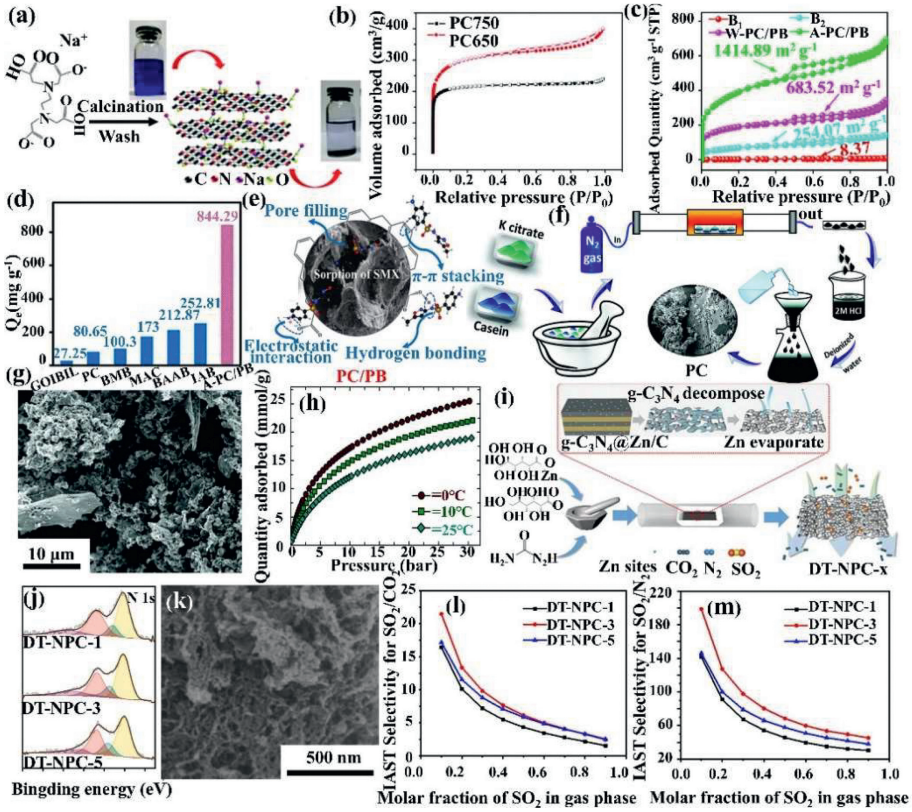


Fig. 7. (a) Schematic illustration of the preparation process and (b) N_2 adsorption-desorption isotherms of PC-650 and PC-750. Reprinted with permission [116]. Copyright 2020, RSC. (c) N_2 adsorption-desorption isotherms and (d) comparison of the adsorption ability of SMX with reported sorbents. (e) Adsorption mechanism of SMX on PC/PB. Reprinted with permission [117]. Copyright 2023, Elsevier. (f) Schematic illustration of the preparation craft of CPCs. (g) SEM images of CPC-3. (h) CO_2 capture capacity of CPC-3 at 0, 10 and 25 °C. Reprinted with permission [118]. Copyright 2021, RSC. (i) Schematic illustration of the preparation craft of DT-NPC-xs. (j) N 1s spectra and (k) SEM images of DT-NPC-5. IAST selectivities for (l) SO_2/N_2 and (m) SO_2/CO_2 at 25 °C and 100 kPa. Reprinted with permission [119]. Copyright 2022, Elsevier.

tion capacity and ultrarapid desalting rate (Figs. S6g and h in Supporting information).

4.3. Peroxymonosulfate activation

Because of the widespread application of refractory organic compounds in industry and daily life, it is inevitably detected in water and wastewater [124,125]. Thus, numerous strategies have been explored to reduce the adverse consequences caused by organic pollutants. Compared with the orthodox crafts, advanced oxidation processes (AOPs), especially the PMS activation that can achieve the pollutant complete degradation. This is due to their robust oxidation capability and versatile adaptability [126]. The current core of PMS activation is to develop catalysts that can generate highly reactive oxygen species [127]. Various advanced transition metal-based catalysts, *e.g.*, Co_3O_4, Fe_3O_4 and FeOOH, have been successively exploited [128]. However, the suboptimal durability and unavoidable metal leaching greatly hindered their application in PMS systems [129]. Notably, OAPCs have obtained more and more attention ascribed to their large S_{BET}, adjustable porous structure and remarkable structural stability.

By $C_6H_5Na_3O_7$ self-activation, Zhang *et al.* [96] synthesized a series of 3D PCs (3DPCs) with interconnected carbon skeletons and abundant intrinsic defects (Fig. 8a). The optimal 3DPC-900 obtained a high S_{BET} of 904.9 m^2/g and large V_{pore} of 0.93 mg/cm^3, favoring exposing more active sites (Fig. 8b). When taken for the phenol degradation, an ultrapid degradation kinetic constant of 1.45 min^{-1} was achieved (Fig. 8c). Moreover, 3DPC-900 also presented a superior degradation efficiency for other pollutants, such as bisphenol A (BPA) and SMX.

Transition metal-doped PCs have many oxidation mechanisms and low secondary pollution, favoring further adding degradation efficiency. Lv *et al.* [130] used $Co(CH_3COO)_2$ and $Zn(CH_3COO)_2$ as Co-/Zn-containing precursors/activators, and polyester waste as carbon sources, fabricating Co/Zn Co-doped PCs (Zn_1Co_5/P_4C). Characterization results indicated that Zn evaporation favored the formation of PC frameworks, and Co nanoparticles can enhance the graphitization degree and act as extra active sites. Notably, levofloxacin degradation efficiency was as high as 96.60 % within 90 min (Fig. 8d). Mechanism analysis revealed that the excellent catalytic efficiency may be because the PC frameworks can effectively support and protect the highly active Co nanoparticles, while the evaporated Zn could increase the S_{BET}.

4.4. Electro-Fenton

EF is an electrochemical AOP technique (EAOPs), having obvious advantages of low cost, high efficiency, high integration and sustainability [131]. EF can *in situ* produce H_2O_2 on the cathode by a selective $2e^-$ oxygen reduction reaction (ORR), thus yielding $^{\bullet}OH$ with highly non-selective oxidation. Thus, the process highly depends on the continuous H_2O_2 generation, which is primarily determined by the cathode materials [132,133]. Carbon-based materials are prominent cathode catalysts so far that have superior S_{BET}, adjustable pore structure, nailing conductivity and high structural stability [134]. However, the orthodox graphene, carbon aerogel and carbon felt are greatly constrained by the inadequate

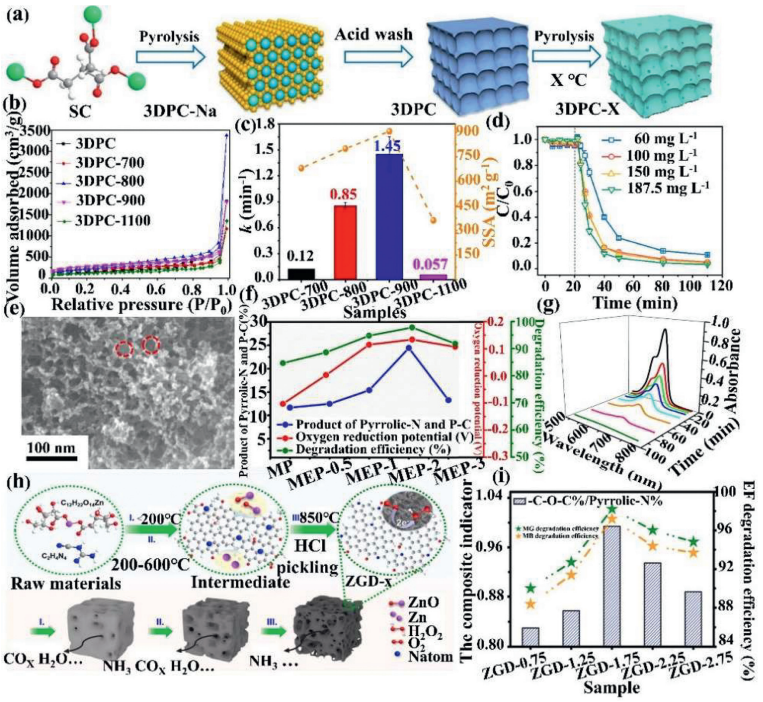


Fig. 8. (a) Scheme of the manufacture process and (b) N_2 adsorption-desorption isotherms of 3DPC-X. (c) The change trend of k and the S_{BET} along with the increased carbonization temperature. Reprinted with permission [96]. Copyright 2022, Elsevier. (d) Influence of Zn_1Co_5/P_4C dosage on the degradation efficiency. Reprinted with permission [130]. Copyright 2023, Elsevier. (e) SEM images of MEP-2. (f) The curves of dependence of pyrrolic-N and P-C (%) on the ORR potential and degradation efficiency. Reprinted with permission [135]. Copyright 2023, Elsevier. (g) UV−vis spectra of degradation of MB driven by DLRD-TENG systems. Reprinted with permission [52]. Copyright 2019, Elsevier. (h) Schematic illustration of the formation mechanism for ZGD-*x*. (i) The influence of indicators on the EF degradation efficiencies for MG and MB. Reprinted with permission [136]. Copyright 2021, Elsevier.

$2e^-$ ORR catalytic activity and selectivity. In constant, OAPCs are suitable catalysts for EF systems.

Chen *et al.* [135] prepared N/P co-doped PCs with unique 3D hierarchical porous structures and copious N (2.9%) and P doping (2.9%) (Fig. 8e). Viewing the synergistic effect of NaH_2PO_2 and EDTA-2K, the generated micro-mesopores from gas templates could well accommodate $^{\bullet}OH$ radicals, and the massive pyrrolic-N and P-C active sites enhance $2e^-$ ORR selectivity. Therefore, when utilized for the MB degradation, the optimal MEP-2 gained a high degradation efficiency of 98.4%, and for mixed dyes was 97.1% (Fig. 8f). To harvest renewable mechanical energy to achieve deeper degradation, Chen *et al.* [52] exploited an double layer rotary disc-structured MB triboelectric nanogenerator (DLRD-TENG). When using DLRD-TENG to drive EF systems that used $C_{10}H_{14}N_2Na_2O_8$ activated taraxacum-derived OAPCs, an ultrahigh degradation efficiency of 96% was achieved (Fig. 8g).

Further, Tian *et al.* [136] proposed a template-assisted self-activation craft to fabricate N/O co-doped mesoporous carbons, where $C_{12}H_{22}O_{14}Zn$ served as self-activators and dicyandiamide acted as gas foaming agents/N sources (Fig. 8h). When taking the DLRD-TENG system, it acquired both high degradation efficiencies of 98.2% and 97.3% for malachite green (MG) and MB, respectively. Mechanism research showed that the excellent property was mainly attributed to high V_{meso}, broad pore size distribution and the optimal N-O configuration (Fig. 8i).

4.5. Microwave absorption

With the wide usage of electronic devices, electromagnetic radiation has become a new pollution source. An effective way to solve the threat is microwave absorption. Microwave absorber (MA) can absorb massive electromagnetic waves and then convert them into other forms of energy dissipation. The performance of MA is dependent on its internal components and microstructure [137]. PCs have copious porosity and periodic structures with micro-distributed units, which can realize deep penetration in the microwave absorption process [138]. However, orthodox PCs are apt for oxidation and degradation [139]. As a better selection, the thermal decomposition of organic salts into highly amorphous carbon and the concomitant generation of reducing gases to rebuild the carbon skeleton help to optimize the pore structure and surface chemical property of OAPCs.

Shen *et al.* [140] prepared 3D interconnected GO nanocapsules (IGNCs) using $C_6H_5Na_3O_7$ self-activation (Figs. S7a and b in Supporting information). Notably, *in situ*-generated Na_2CO_3 can be evenly distributed in the carbon substrate, favoring the porosity formation. Thus, IGNCs gained massive oxygen-containing groups and copious disorder degrees, which not only enhanced the impedance matching characteristics but also enhanced the dipole and favored the amplified polarization loss capacity. As a result, it illustrated an effective absorption bandwidth (EAB) of 4.32 GHz, at a fill concentration of only 5 wt% and a matched thickness of 2.3 mm (Figs. S7c and d in Supporting information).

Innovatively, by the direct pyrolysis of $C_6H_5K_3O_7$ in sealed tubes with diverse volumes, Hou *et al.* [141] fabricated a series of rich-defect PCNs (S-PCNs) (Fig. S7e in Supporting information). The optimal S-PCN-3 with clear micro-mesopore structures gained a large S_{BET} of 825.6 m^2/g and ultrahigh disorder degree (Figs. S7f-h in Supporting information). Study displayed that the induced defective carbon structures can effectively enhance microwave absorption. Thereby, S-PCN-3 acquired a remarkable electromagnetic wave absorption property, with a reflection loss of up to −58.2 dB and an effective EAB of 3.2 GHz, even at an ultra-low filler content of 5 wt% (Fig. S7i in Supporting information).

5. Challenges and prospects

Although there have been widely investigations on developing advanced OAPCs for treating various environmental applications, further research is required to sufficiently understand the drawbacks of OAPCs and how to further effectively reinforce them to maximize the material performance.

(1) In the future, it is vital to develop magnetic or self-supporting OAPCs to realize their effective performance release and rapid material recovery. For non-electrochemical applications, OAPCs own a strong ability, however, a tedious recovery step is often required, especially for particles with small sizes and low density. This greatly adds to the overall treatment cost. Thus, introducing magnetic particles into OAPCs is necessary, which can not only solve the recycling issues and improve the reusability of OAPCs. To meet all the applications, more advocacy is to construct self-supported OAPCs. This is similar to activated carbon fiber and activated carbon cloth, which contain 100% active material and copious porosity. Currently, constructing carbon aerogel-based or wood-based OAPCs is an important research direction.

(2) In the future, a deeper understanding of the basic theories of OAPCs is required. In-depth research on the decomposition and activation mechanisms of organic salts, clarifying the reaction processes of diverse organic salts at the atomic and molecular levels, will help to more precisely regulate the synthesis (reasonable hierarchical porous structure, ample ion/molecule accessible surface, copious defect degrees, appropriate heteroatom doping and superior mass/charge transfer efficiency) of OAPCs to meet diverse applications. Advanced *in situ* characterization techniques, *e.g.*, *in-situ* SEM, *in-situ* FTIR and *in-situ* Raman, can monitor the structural evolution of organic salts during the activation process in real-time, providing direct evidence for optimizing the synthesis process.

(3) Currently, artificial intelligence has been extensively applied in pharmaceutical research. As one subset, machine learning (ML) enables computer software to predict outcomes without the need for massive programming. A key characteristic of ML lies in its capability to train algorithms for handling complex and large-scale multidimensional datasets. Although existing studies have proved the application of ML in OAPCs for environmental remediation, this field remains in the early development stage. ML-based prediction models hold the potential to greatly reduce research workloads, making it worthwhile to explore the comprehensive application of ML in composite material combination prediction and production condition prediction.

6. Conclusion

Overall, this review overviews sustainable OAPCs, stressing their multiple roles as activators and self-activators. Six diverse organic salts are comprehensively analyzed and identified for their unique decomposition pathways and activation mechanisms. Notably, structural control of OAPCs from 0D to 3D is discussed by regulating the precursor chemistry and pyrolysis conditions, optimizing ion transport and surface accessibility. Eventually, the environmental applications of OAPCs are assessed, proving superior application potential in various fields, such as adsorption, CDI, PMS activation, EF and microwave absorption. New manufacturing and recovery craft, advanced characterization methods and ML prediction are vital for the future development. We underline that the collaboration of researchers from diverse fields will further reinforce the scientific understanding of OAPCs and promote practical applications.

CRediT authorship contribution statement

Mingxing Shi: Writing – review & editing, Visualization, Funding acquisition, Conceptualization. **Jiahui Liu:** Writing – original draft, Visualization, Software. **Wei Jin:** Writing – review & editing, Funding acquisition. **Zahira Bano:** Writing – review & editing, Supervision, Software. **Yubo Pan:** Visualization, Software. **Jianzhe Ma:** Writing – review & editing. **Xu Wu:** Writing – review & editing, Software. **Huijuan Jia:** Supervision, Funding acquisition. **Guolin Tong:** Supervision, Project administration, Funding acquisition.

Declaration of competing interest

The authors declare that they have no known competing financial interests or personal relationships that could have appeared to influence the work reported in this paper.

Acknowledgments

The authors would like to acknowledge the financial support of the Natural Science Foundation of Jiangsu Province (No. BK20250707), Postgraduate Research & Practice Innovation Program of Jiangsu Province (No. KYCX25_1494), Nanjing Forestry University High-level Talent Scientific Research Start-up Foundation (No. 163105774) and Suzhou Project (No. ZXL2024374).

Supplementary materials

Supplementary material associated with this article can be found, in the online version, at doi:10.1016/j.cclet.2026.112411.

References

[1] J.L. Carrillo, A.A. Ezazi, S. Perez-Beltran, et al., Chem 111 (2025) 102486.
[2] Y. Pan, R. Che, K. Lu, et al., Chem. Eng. J. 508 (2025) 161229.
[3] D. Jiang, R. Xu, L. Bai, et al., Coord. Chem. Rev. 516 (2024) 215923.
[4] K. Chen, S.H. Mousavi, R. Singh, et al., Chem. Soc. Rev. 51 (2022) 1139–1166.
[5] L. Men, H. Lin, L. Zhu, et al., ACS Sust. Chem. Eng. 12 (2024) 8780–8791.
[6] J. Lu, Z. Xiong, M. Sakil, et al., J. Hazard. Mater. 471 (2024) 134464.
[7] J. Wang, S. Zhuang, Coord. Chem. Rev. 400 (2019) 213046.
[8] L. Men, S. Feng, J. Zhang, et al., Green Chem. 26 (2024) 1170–1193.
[9] M. Shi, K. Lu, H. Jia, et al., Sci. Total. Environ. 904 (2023) 167339.
[10] V. Pavlenko, S. Żółtowska, A. Haruna, et al., Mat. Sci. Eng. R 149 (2022) 100682.
[11] H. Qiang, M. Shi, Y. Pan, et al., Sep. Purif. Technol. 361 (2025) 131294.
[12] D. Barker, J. Chen, Z. Wan, et al., Chem. Soc. Rev. 54 (2025) 623–652.
[13] I. Alali, A. Shehu, R. Mokaya, et al., Energy. Environ. Sci. 17 (2024) 5024–5038.
[14] H. Qiang, M. Shi, K. Lu, et al., Desalination 593 (2025) 118246.
[15] Z. Yu, B. Qin, Z.Y. Ma, et al., Adv. Mater. 31 (2019) 1900651.
[16] H. Wang, Y. Shao, S. Mei, et al., Chem. Rev. 120 (2020) 9363–9419.
[17] R. Ding, Y. Zhou, Y. Zhang, et al., Adv. Funct. Mater. 35 (2025) 2415006.
[18] M. Mudassir, S. Kousar, M. Ehsan, et al., Renew. Sust. Energy Rev. 185 (2023) 113594.
[19] R. Chakraborty, K. Vilya, M. Pradhan, et al., J. Mater. Chem. A 10 (2022) 6965–7005.
[20] L. Men, B. Luo, L. Zhu, et al., Chem. Eng. J. 513 (2025) 163013.
[21] C. Yang, Y. Wang, M. Liang, et al., Appl. Catal. B: Environ. 323 (2023) 122133.
[22] B. Xue, C. Liu, X. Wang, et al., Chem. Eng. J. 480 (2024) 147994.
[23] D. Wang, H. Dong, D. Zhang, et al., Int. J. Biol. Macromol. 305 (2025) 141361.
[24] H. Qiang, M. Shi, F. Wang, et al., Sep. Purif. Technol. 333 (2024) 125915.
[25] H. Arslanoğlu, J. Hazard. Mater. 374 (2019) 238–247.
[26] L. Hao, J. Wen, Z. Yun, et al., Carbon 128 (2018) 97–105.
[27] P. Li, P. Liu, H. Liu, et al., J. Energy Storage 121 (2025) 116349.
[28] B. Yang, J. Chen, S. Lei, et al., Adv. Energy Mater. 8 (2018) 1702409.
[29] X. Wu, J. Liu, Y. Wang, et al., Chem. Eng. J. 512 (2025) 162487.
[30] Y. Yao, Y. Yu, Y. Liu, et al., J. Energy. Storage. 74 (2023) 109261.
[31] S. Yu, N. Sun, L. Hu, et al., J. Power Sources 405 (2018) 132–141.
[32] M. Shi, K. Lu, X. Hong, et al., Chem. Eng. J. 471 (2023) 144465.
[33] L. Hou, W. Yang, B. Jiang, et al., Carbon 183 (2021) 176–186.
[34] M. Sevilla, ACS Nano 8 (2014) 5069–5078.
[35] M. Shi, X. Hong, C. Liu, et al., Chem. Eng. J. 453 (2023) 139764.

[36] Y. Wang, Y. Liu, X. Huang, et al., Chin. Chem. Lett. 35 (2024) 109301.
[37] S. Tian, J. Dai, Y. Jiang, et al., J. Colloid. Interf. Sci. 505 (2017) 858–869.
[38] M. Shi, H. Jia, J. Liu, et al., Coordin. Chem. Rev. 543 (2025) 216949.
[39] B. Qi, J. Wang, H. Sun, et al., Sep. Purif. Technol. 382 (2025) 136012.
[40] X. Shi, C. Zhou, Y. Gao, et al., Carbon Energy 6 (2024) 534.
[41] X. Wu, B. Ding, C. Zhang, et al., Carbon 153 (2019) 225–233.
[42] Y. Feng, G. Li, X. Wu, et al., J. Porous Mater. 30 (2023) 2113–2120.
[43] G. Singh, I. Ismail, C. Bilen, et al., Appl. Energy 255 (2019) 113831.
[44] H. Liao, L. Zhong, H. Zeng, et al., Carbon 213 (2023) 118305.
[45] M. Xia, W. Chen, J. Wu, et al., Fuel 291 (2021) 120185.
[46] W. Yue, Z. Yu, X. Zhang, et al., J. Anal. Appl. Pyrolysis 178 (2024) 106409.
[47] W. Hui, F. Mao, W. Xiang, et al., Compos. Commun. 28 (2021) 100961.
[48] Y. Shi, J. Zhu, G. Yuan, et al., Chem. Eng. J. 386 (2020) 124009.
[49] S. Sun, B. Ding, R. Liu, et al., J. Alloys Compd. 803 (2019) 401–406.
[50] T. Lu, J. Bai, M. Demir, Sep. Purif. Technol. 296 (2022) 121368.
[51] G. Tan, X. Li, D. Xiao, New J. Chem. 44 (2020) 4071–4080.
[52] Y. Chen, Y. Zhu, M. Tian, et al., Nano Energy 59 (2019) 346–353.
[53] M. Taha, S. Anwar, M. Ramadan, et al., Desalination 511 (2021) 115099.
[54] G. Tan, Q. Liu, X. Li, et al., Appl. Surf. Sci. 496 (2019) 143526.
[55] S. Song, Y. Wang, P. Tian, et al., Int. J. Hydrogen. Energy 47 (2022) 24728–24737.
[56] M. Jafari, G. Botte, ACS Omega 9 (2024) 13134–13147.
[57] W. Yang, W. Yang, F. Ding, et al., Carbon 111 (2017) 419–427.
[58] J. Liu, X. Mei, F. Peng, et al., Chin. Chem. Lett. 34 (2023) 108187.
[59] S. Kang, D. Wang, M. Ma, et al., Bioresource. Technol. 442 (2026) 133695.
[60] R. Sun, Y. Chen, X. Gao, et al., J. Energy. Storage 91 (2024) 112025.
[61] S. Liu, S. Wu, H. Cheng, et al., Ind. Crops Prod. 179 (2022) 114657.
[62] M. Shi, X. Liu, H. Jia, et al., Sep. Purif. Technol. 330 (2024) 125354.
[63] K. Lu, H. Jing, H. Jia, et al., J. Colloid. Interf. Sci. 679 (2024) 262–272.
[64] J. Zhu, D. Xu, W. Qian, et al., Small 12 (2016) 1935–1944.
[65] Z. Wang, C. Liu, O. Jia, et al., Ind. Crop. Prod. 227 (2015) 120808.
[66] W. Qian, J. Zhu, Y. Zhang, et al., Small 11 (2015) 4959–4969.
[67] N. Sun, X. Zhang, C. Zhao, et al., ChemElectroChem 5 (2018) 3873–3880.
[68] G. Duan, L. Zhao, C. Zhang, et al., Diamond. Relat. Mater. 129 (2022) 109339.
[69] G. Duan, J. Xiao, L. Chen, et al., J. Energy. Storage. 67 (2023) 107559.
[70] Y. Gao, S. Zhang, X. Li, et al., Carbon 181 (2021) 323–334.
[71] Y. Zhang, G. Ji, C. Li, et al., Chem. Eng. J. 390 (2020) 124398.
[72] L. Wan, P. Song, J. Liu, et al., J. Power. Sources 438 (2019) 227013.
[73] P. Nie, X. Shang, B. Hu, et al., J. Colloid. Interf. Sci. 612 (2022) 277–286.
[74] J. Shi, J. Xu, H. Cui, et al., Sep. Purif. Technol. 355 (2025) 129756.
[75] S. Gu, Y. Wang, D. Zhang, et al., Chemosphere 289 (2022) 133148.
[76] S. Zhe, L. Xiong, W. Hao, et al., J. Energy. Storage 515 (2021) 230629.
[77] L. Hu, L. Ma, Q. Zhu, et al., New J. Chem. 22 (2017) 13185–14002.
[78] Z. Hui, Z. Yi, L. Qing, et al., Appl. Energy. 306 (2021) 118131.
[79] T. Sun, C. Wang, D. Jiao, et al., J. Mater. Sci.: Mater. Electron. 28 (2017) 8993–9002.
[80] J. Zhu, D. Xu, C. Wang, et al., Carbon 115 (2017) 1–10.
[81] D. Cheng, M. Tian, B. Wang, et al., J. Colloid. Interf. Sci. 572 (2020) 216–226.
[82] H. Qiang, M. Shi, F. Wang, et al., Sep. Purif. Technol. 308 (2023) 122918.
[83] X. Yu, J. Zhao, R. Lv, et al., J. Mater. Chem. A 36 (2015) 18313–18736.
[84] X. Zhao, H. Chen, F. Kong, et al., Chem. Eng. J. 364 (2019) 226–243.
[85] Z. Chen, C. Feng, W. Li, et al., Chin. J. Catal. 39 (2018) 841–848.
[86] S. Chongdar, R. Chatterjee, S. Reza, et al., Adv. Energy. Mater. 15 (2024) 2403809.
[87] R. Ding, F. Zeng, H. Zhao, et al., Compos. Part. B 288 (2024) 111932.
[88] J. Pang, W. Zhang, H. Zhang, et al., Carbon 132 (2018) 280–293.
[89] H. Zhao, P. Lu, F. Chen, et al., Chin. Chem. Lett. 35 (2024) 108694.
[90] Y. He, D. Gehrig, F. Zhang, et al., Adv. Funct. Mater. 26 (2016) 8255–8265.
[91] L. Yao, B. Zhan, X. Qi, et al., J. Mater. Sci. Technol. 224 (2024) 56–65.
[92] Y. Zhao, X. Zuo, Y. Guo, et al., Nano. Micro. Lett. 13 (2021) 144.
[93] W. Zhang, H. Li, D. Feng, et al., Carbon Energy 6 (2024) 461.
[94] G. Liu, X. Li, M. Liu, et al., SusMat 3 (2023) 834–842.
[95] X. Chen, L. Xu, L. Zeng, et al., Dalton Trans 41 (2020) 14299–14708.
[96] Z. Hang, G. Xiao, C. Shuo, et al., Sep. Purif. Technol. 292 (2022) 121048.
[97] J. Earnshaw, A. Ashok, K. Leong, et al., Small 21 (2024) 2406174.
[98] C. Li, E. Zhou, Z. Yu, et al., Appl. Catal. B: Environ. 269 (2020) 118771.
[99] W. Eom, A. Kim, H. Park, et al., Adv. Funct. Mater. 26 (2016) 7605–7613.
[100] C. Zhao, L. Shan, R. Sun, et al., Mater. Today 81 (2024) 104–117.
[101] L. Dong, J. Yang, M. Chhowalla, et al., Chem. Soc. Rev. 46 (2017) 7097–7472.
[102] M.J. Yoo, H.B. Park, Carbon 141 (2019) 515–522.
[103] Y. Zhang, Z. Wang, D. Li, et al., J. Mater. Chem. A 8 (2020) 22874–22885.
[104] L. Chen, J. Sun, J. Dai, et al., J. Taiwan Inst. Chem. Eng. 95 (2018) 660–668.
[105] Q. Luo, Q. Chen, Y. Wang, et al., Chem. Eng. J. 420 (2021) 130483.
[106] L. Hou, W. Yang, Y. Li, et al., Chem. Eng. J. 417 (2021) 129289.
[107] F. Li, J. Jiang, J. Wang, et al., Nano Res 16 (2022) 127–145.
[108] B. Xue, J. Xu, Y. Feng, et al., J. Colloid. Interf. Sci. 642 (2023) 736–746.
[109] M. Zhang, H. Ling, T. Wang, et al., Nano-Micro Lett. 14 (2022) 157.
[110] Q. Wang, Y. Qu, Y. Yuan, et al., Adv. Mater. 37 (2025) 2418997.
[111] Z. Zhao, S. Das, G. Xing, et al., Angew. Chem. Int. Ed. 57 (2018) 11952–11956.
[112] T. Wang, L. Peng, B. Deng, et al., Fuel 357 (2024) 129653.
[113] X. Zhu, Y. Gao, Q. Yue, et al., J. Taiwan Inst. Chem. Eng. 85 (2018) 141–148.
[114] H. Jia, H. Xu, M. Shi, et al., J. Colloid. Interf. Sci. 650 (2023) 1152–1163.
[115] H. Jia, H. Xu, M. Shi, et al., Sep. Purif. Technol. 325 (2023) 124652.
[116] G. Tan, X. Li, D. Xiao, et al., New J. Chem. 44 (2020) 4071–4080.
[117] J. Qin, R. Ji, Q. Sun, et al., Bioresour. Technol. 369 (2022) 128361.
[118] G. Singh, R. Bahadur, A.M. Ruban, et al., Green Chem. 23 (2021) 5571–5583.
[119] Q. Zhu, F. Li, Y. Zheng, et al., Sep. Purif. Technol. 284 (2022) 120272.
[120] Q. Ma, Z. Wang, L. Zhang, et al., Sep. Purif. Technol. 353 (2025) 128503.
[121] B. Xiao, L. Zhang, Q. Ma, et al., Desalination 612 (2025) 118955.
[122] Z. Guo, G. Shen, Z. Wang, et al., Desalination 576 (2024) 117329.
[123] Y. Liu, L. Wang, Q. Ma, et al., Nat. Commun. 15 (2024) 10175.
[124] X. Wang, Z. Li, R. Gao, et al., Environ. Sci. Technol. 58 (2024) 17190–17200.
[125] Y. Chai, F. Wang, Y. Gao, et al., Environ. Res. 282 (2025) 122099.
[126] B. Hua, L. Zheng, A. Awomuti, et al., Chem. Eng. J. 443 (2022) 136439.
[127] A. Pophali, K. Lee, L. Zhang, et al., Chem. Eng. J. 373 (2019) 365–374.
[128] Y. Liu, X. Niu, X. Yang, et al., Chem. Eng. J. 489 (2024) 151417.
[129] G. Jin, Y. Ping, C. Yi, et al., Chin. Chem. Lett. 33 (2022) 4792–4797.
[130] H. Lv, Y. Huo, M. Cheng, et al., Chemosphere 335 (2023) 139020.
[131] S.O. Ganiyu, M. de Araújo, E. Costa, et al., Appl. Catal. B: Environ. 283 (2020) 119652.
[132] S. Zheng, Z. Yuan, D. Dionysiou, et al., Chem. Eng. J. 458 (2023) 141471.
[133] G. Zhu, X. Fan, Y. Yu, et al., Environ. Sci. Technol. 58 (2024) 19093–19570.
[134] J. Chen, W. Ren, S. Zhong, et al., Chem. Eng. J. 500 (2024) 157125.
[135] C. Chen, M. Tian, H. Han, et al., Electrochim. Acta 389 (2021) 138732.
[136] M. Tian, Y. Zhu, Y. Chen, et al., Nano Energy 83 (2021) 105825.
[137] Z. Wang, X. Liu, G. Zhang, et al., Ceram. Int. 49 (2023) 35885–35897.
[138] R. Ding, Y.Q. Wang, F. Zeng, et al., Small 19 (2023) 2302132.
[139] S. Sharma, S. Parne, S. Panda, et al., Adv. Colloid. Interf. Sci. 327 (2024) 103143.
[140] X. Shen, K. Ran, B. Zheng, et al., Inorg. Chem. Commun. 153 (2023) 110863.
[141] H. Liqiang, Y. Wang, J. Bo, et al., Carbon 183 (2021) 176–186.